



HAL
open science

CuO-CeO₂ catalysts based on SBA-15 and SBA-16 for COPrOx. Influence of oxides concentration, incorporation method and support structure

Inés S. Tiscornia, Albano M. Lacoste, Magali Bonne, Bénédicte Lebeau, Alicia V. Boix

► **To cite this version:**

Inés S. Tiscornia, Albano M. Lacoste, Magali Bonne, Bénédicte Lebeau, Alicia V. Boix. CuO-CeO₂ catalysts based on SBA-15 and SBA-16 for COPrOx. Influence of oxides concentration, incorporation method and support structure. *Catalysis Today*, In press, 10.1016/j.cattod.2021.08.008 . hal-03425636

HAL Id: hal-03425636

<https://hal.science/hal-03425636>

Submitted on 30 Nov 2021

HAL is a multi-disciplinary open access archive for the deposit and dissemination of scientific research documents, whether they are published or not. The documents may come from teaching and research institutions in France or abroad, or from public or private research centers.

L'archive ouverte pluridisciplinaire **HAL**, est destinée au dépôt et à la diffusion de documents scientifiques de niveau recherche, publiés ou non, émanant des établissements d'enseignement et de recherche français ou étrangers, des laboratoires publics ou privés.

**CuO-CeO₂ catalysts based on SBA-15 and SBA-16 for COPrOx.
Influence of oxides concentration, incorporation method and
support structure.**

Inés S. Tiscornia^{a*}, Albano M. Lacoste^a, Magali Bonne^{b,c}, Bénédicte Lebeau^{b,c}, Alicia V. Boix^a

*^aInstituto de Investigaciones en Catálisis y Petroquímica, INCAPE (FIQ, UNL-CONICET),
3000 Santa Fe, Argentina.*

^bUniversité de Haute Alsace (UHA), CNRS, IS2M UMR 7361, 68100 Mulhouse, France.

^cUniversité de Strasbourg, F-67000 Strasbourg, France.

*Contact author information: Inés S. Tiscornia

e-mail: itiscornia@fiq.unl.edu.ar

Full postal address: INCAPE. Santiago del Estero 2829 - (3000) Santa Fe, Argentina

Phone number: +54-342-4536861

Submitted to: Catalysis Today

Abstract

In this work different variables that can affect the catalytic behavior of CuO-CeO₂ supported on mesoporous silica (SBA-15 and SBA-16) were studied. The influence on the COPrOx

activity of the relative concentration of the CuO and CeO₂ active phase and different impregnation methods in mesoporous support was analyzed. The physicochemical characterization was performed EDS-SEM and TEM-STEM, N₂ isotherms, X-ray Diffraction (XRD) and X-ray Photoelectron Spectroscopy (XPS). The incipient wetness impregnation method (IWI) was the better alternative to introduce the active phases compared to solid state impregnation (SSI). In addition, the catalysts based on 2-D structure of SBA-15 were more active and selective than those based in 3-D SBA-16. In general, the high surface area of the supports benefited the dispersion of CuO and CeO₂ oxides nanoparticles. All catalysts displayed the preservation of the mesostructure and the formation of nanoparticles of active phases (less than 10 nm) detected by TEM. The best COPrOx catalyst, obtained from the SBA-15 fibers by IWI method, with a relative CuO concentration of 0.2, exhibited X_{CO} ≥ 99 % at 175 °C and above 90 % in a wide window of temperatures. This catalyst showed an adequate performance in presence of CO₂ and H₂O and good recovery of CO conversion and selectivity. The analysis by XPS revealed that the majority species were Ce⁴⁺, however in some catalysts Ce³⁺ species are also present, which are associated with vacancies oxygen and favor the redox process. In addition, Cu²⁺ and Cu⁺ species are present, the latter recognized as a key site of CO adsorption in the reaction mechanism.

Keywords: COPrOx, impregnation methods, active phase concentration, porous mesostructure, SBA-15/SBA-16

1. Introduction

The growth in world energy demand, the decrease in fossil fuel sources and the emission of greenhouse gases have prompted the scientific community to search for alternative sources of energy that are environmentally friendly [1,2]. All major sectors in the hydrocarbon economy can progress towards decarbonization with a deployment of H₂ technologies [3].

Significant progress was made in the development of H₂-powered fuel cells to produce energy with higher electrical efficiencies compared with internal combustion engines. Among several types of fuel cells, proton exchange membrane fuel cells (H₂-PEMFC) are considered to be the most technically advanced for such application [4].

Hydrogen produced by means of the steam reforming or autothermal process of hydrocarbons or alcohols should contain less than 10 ppm of carbon monoxide before entering the cell, since CO poisons the Pt anode of the fuel cells. After the reforming step, the hydrogen production process continues with the water gas shift reaction (WGSR), where the stream is enriched in hydrogen and the CO content is diminished to 1 %. As the CO concentration in the hydrogen stream is so high to enter to the cell, it is necessary to reduce it to the desired levels.

Among different strategies, such as pressure swing adsorption, hydrogen membrane separation, selective CO methanation and CO preferential oxidation (COPrOx), the latter is considered as an alternative adequate due to its simplicity and effectiveness. By applying appropriate catalysts, it may be possible to reduce the concentration of carbon monoxide in the H₂ stream with the lowest consumption of hydrogen and mild operation conditions (atmospheric pressure and temperatures below 200 °C). In this sense, several catalysts with high efficiency and selectivity in a broad temperature range have been studied with promising

results [5]. Noble metal-based catalysts have been extensively studied for more than two decades. Many efforts have been devoted to improving the low-temperature performance of supported Pt or bimetallic systems [6–9], as well also Au based catalysts [10,11] and more recently the Au/TiO₂ in photo-assisted preferential CO oxidation [12–14]. However, the high cost of noble metals led the investigations toward the use of other active phases. In this vein, numerous articles on transition metal-ceria systems have been published, in which CeO₂ plays a fundamental role in redox reactions due to its facility to release and storage oxygen [15,16].

Likewise, the CuO-CeO₂ system has also been widely studied by several authors and the results obtained in COPrOx are comparable to those reached by noble catalysts on a great number of occasions. In this sense, the CuO/CeO₂ system performance depends of the diverse factors, such as the preparation methods, the concentrations of actives phases, the promoters, etc., since this influence in the physicochemical properties affecting the Cu⁺/Cu²⁺ and Ce³⁺/Ce⁴⁺ redox couples [17–23]. The relative high reactivity of CuO-CeO₂ catalysts towards CO rather than H₂ oxidation is attributed to the synergistic copper-ceria interactions on the interface. It is generally accepted that the preferentially adsorbed CO on Cu migrates to the Cu-Ce interfaces and reacts with the lattice oxygen provided by the CeO₂ support, following a Mars van Krevelen mechanism [24].

On the other hand, CuO-CeO₂ systems dispersed in a suitable support have been less studied. This procedure could favor the dispersion of the active phase and decrease the necessary amount of precursors used in the preparation of the catalyst. In this vein, different oxides such as Al₂O₃, ZrO₂, SiO₂ and mesoporous silica were used to prepare CO oxidation catalysts [25–27].

In our previous work, the performance in COPrOx of powder and monolithic catalysts based on CuO-CeO₂ supported on silica with different morphology and textural properties were studied [28]. In particular, mesoporous silicas offer a well-defined structure with high surface area and voluminous pores where the active phases could be located [29,30].

The goal of this work was to study different variables that can affect the catalytic behavior of CuO-CeO₂ supported on mesoporous silica (SBA-15 and SBA-16). The influence on the COPrOx activity of the relative concentration of the CuO and CeO₂ active phases and different impregnation methods in mesoporous support was analyzed. In addition, the physicochemical characterization of catalysts was performed by electron microscopies (SEM and TEM), N₂ adsorption-desorption isotherms, X-ray Diffraction (XRD) and X-ray Photoelectron Spectroscopy (XPS).

2. Materials and methods

2.1 Supports and catalysts synthesis

Synthesis of SBA-15 and SBA-16. SBA-15 fibers were obtained according to a typical synthesis method [31]. A solution was prepared with the following molar ratio: 1.0 TEOS:0.017 P123:5.6 HCl:197 H₂O, where Pluronic P123 (average Mn ~5800 g mol⁻¹, Sigma-Aldrich[®]) was used as the structure directing agent and tetraethyl orthosilicate (TEOS, reagent grade, 98 %, Sigma-Aldrich[®]) as the silica source. The mixture was stirred at 45 °C for 7.5 h and then was aged in an oven at 80 °C for 15.5 h. The solid was recovered by filtration, washed with distilled water and dried at 60 °C.

In order to obtain short rods of SBA-15 a similar procedure to previous one was followed, but TEOS was added drop by drop and the ripening step was done under static conditions. Finally, both materials were calcined in air for 6 h at 550 °C in a muffle furnace to remove the surfactant from the pores. These mesoporous synthesized were labeled as S15/F and S15/R for fibers and rods morphology, respectively.

On the other hand, SBA-16 spheres were prepared from a solution with the following molar ratio: 1.0 TEOS:0.0033 F127:5.6 HCl:171 H₂O, where F127 (average Mn ~12600 g mol⁻¹, Sigma-Aldrich®) was the surfactant used. The acidic solution of F127, H₂O and HCl was stirred until complete dissolution of Pluronic at 60 °C; then, TEOS was added drop by drop. Single stage of ripening-ageing was carried out in an oven at 80 °C for 24 h in quiescent conditions.

Irregular particles of SBA-16 were synthesized from a solution with composition 1.0 TEOS:0.0032 F127:0.88 HCl:1.72 BuOH:111 H₂O, where n-butanol was added as co-surfactant [32]. After stirring at 45 °C for 24 h the mixture was transferred to an autoclave and aged in an oven at 100 °C for 24 h. Also, the last steps of filtration, washing and calcination processes were followed to obtain the final materials. The powders obtained were denoted as S16/S and S16/I for spherical and irregular morphology.

Incorporation of CuO and CeO₂. Active oxides CuO and CeO₂ were incorporated on the silica supports by two methods, incipient wetness impregnation (IWI) and solid state impregnation (SSI). In the first method, solutions were prepared with the appropriate concentration of precursor salts, Cu(NO₃)₂·3H₂O and Ce(NO₃)₃·6H₂O (Sigma-Aldrich), co-dissolved in minimum amount of ethanol. Another material was also obtained by IWI method

from a solution consisting of commercial colloidal dispersed CeO₂ (Nyacol[®], acetate stabilizer) and Cu(CH₃COO)₂·H₂O (Merck).

In the solid state impregnation, precursor salts and the silica support were mixed in a mortar and subsequently introduced in the zirconia crucibles of the ball mill equipment (Phillips Minimill). The mixtures were grinded for 30 min. Finally, all solids were calcined in air flow at 450 °C to remove anionic precursors. The catalysts prepared were labeled as S15/ or S16/M-x-Y, where “M” refers to their morphology, “x” to relative CuO concentration and “Y” to the impregnation method.

For comparison, a CuO-CeO₂ bulk catalyst was prepared by the coprecipitation method with CuO 20 wt. % from an aqueous solution of copper and cerium nitrate. Then, a solution of sodium hydroxide 1M was added dropwise to the nitrates mixture until pH=10. After stirring for 4 h the precipitate was filtrated, washed and dried. The material was calcined in air flow at 450 °C. This unsupported catalyst was labeled as Bulk-0.20. In addition, a monometallic sample of cerium nitrate impregnated on SBA-15 fibers was prepared by IWI (~ 19 wt. % CeO₂, S15/F-Ce).

2.2 Catalytic tests

COPrOx tests were carried out at atmospheric pressure, approximately 0.2 g of catalyst was loaded in a tubular quartz reactor (15.6 mm i.d.). The gaseous reaction mixture is composed of CO 1 vol. %, O₂ 1 vol. % and H₂ 40 vol. %, He balance, with weight/total flow ratio of 2.3 mg_{cat} min mL⁻¹ (STP) (contact time $\tau = 0.138 \text{ g}_{\text{cat}} \text{ s mL}^{-1} \text{ STP}$). The temperature was varied from 125 to 225 °C, the measurements were performed when the steady state was

achieved. The effect on the activity of CO₂ and H₂O was examined in a separate experiment with the addition of 10 vol. % CO₂ and 10 vol. % H₂O for a selected catalyst. A time-on-stream experiment was performed at 175 °C during 60 h under different reaction conditions. The CO and O₂ conversion and the O₂ selectivity towards CO₂ were defined according to Equation (1), Equation (2) and Equation (3), respectively:

$$X_{CO}(\%) = \frac{[CO]^0 - [CO]}{[CO]^0} 100 \quad (1)$$

$$X_{O_2}(\%) = \frac{[O_2]^0 - [O_2]}{[O_2]^0} 100 \quad (2)$$

$$S_{CO_2}(\%) = 0.5 \frac{[CO]^0 - [CO]}{[O_2]^0 - [O_2]} 100 \quad (3)$$

where [CO] and [O₂] were reactor exit concentrations and [CO]⁰, [O₂]⁰ represented feed concentrations.

Shimadzu chromatograph GC-2014 with a thermal conductivity detector (TCD) equipped with a 5A molecular sieve column was used to analyze the outlet composition gases. The mass balance was closed within ±4%.

2.3 Characterization

JEOL transmission electron microscope JEM-2100 plus model, equipped with EDS detector Oxford X-MAX 65 T model, was used to examine silica supports mesostructure, as well as morphology and size distribution of nanoparticles oxide (TEM technique). The accelerating voltage was 200 kV. In addition, Scanning Transmission Electron Microscopy (STEM) images were obtained in high angle annular dark-field (HAADF) mode. Samples were

prepared dispersing the powder in ethanol and depositing it on Formvar/Carbon in square mesh Cu or Ni. Scanning electron microscopy images of powders were obtained using a Phenom ProX microscope, operated at 15 kV (SEM). EDS analyses were performed employing a fully integrated detector and software of the aforementioned microscope. A second microscope JEOL model JSM-7900F was used for additional analyses, with a BRUKER QUANTAX EDS.

The textural properties were obtained from N₂ adsorption-desorption isotherms (at 77 K) measured with Micrometrics ASAP 2020 equipment. Before the analysis, materials were degassed at 170-200 °C for 8 h. The specific surface area was calculated by BET method and the total pore volume was measured at the P/P⁰ = 0.97 single point. BJH method modified by Kruk, Jaroniec and Sayari (BJH-KJS) [33] was employed to determine the pore size distribution (PSD).

Crystalline phases were characterized by X-ray diffraction (XRD). The measurements were collected on a Shimadzu XD-D1 with monochromatic Cu-K α radiation and a Ni filter at a scanning rate of 2° min⁻¹ in 2 θ = 10-70°. The obtained diffraction peaks were compared to standards published by JCPDS data (Joint Committee on Powder Diffraction Standards).

X-ray Photoelectron Spectroscopy (XPS) analyses were performed in a multi-technique equipment, and the chemical state and relative abundance of copper and cerium species on the surface were studied. The SPECS system is equipped with a dual Mg/Al X-rays source and a hemispherical PHOIBOS 150 analyzer operating in the fixed analyzer transmission mode. The spectra were obtained using a pass energy of 30 eV and the X-ray source was operated at 200 W and 12 kV. The working pressure in the main chamber was less than 2×10⁻⁶ Pa. For the quantitative analysis, the regions corresponding to Ce 3d, Cu 2p, C 1s, O 1s and

Si 2p core levels were recorded for each sample. The Si 2p signal at 103.4 eV (binding energy, B.E.) was taken as internal reference. The data were processed with the Casa XPS program (Casa Software Ltd, UK). The peaks were considered a mixture of Gaussian and Lorentzian functions. For the quantification of the elements, sensitivity factors provided by the manufacturer were employed.

3. Results and Discussion

3.1 Support synthesis and characterization

TEM images of the porous structures of SBA-15 and SBA-16 mesoporous supports are shown in Figure 1. SBA-15 with 2-D mesostructure presents a hexagonally close-packed cylinder-like pore channels, ascribed to $p6mm$ space group. Moreover, the image confirmed the symmetrical pore arrays along [001] direction. Regarding SBA-16, with cubic cage-structured, consists of two non-interpenetrating 3-D channel systems with spherical cavities at the intersection of the channels. The TEM image revealed the characteristic cubic $Im3m$ structure along the [100] direction. In addition, the pore size of mesoporous silicas was estimated from different TEM images, diameters around 7.5 and 6.7 nm were measured for SBA-15 and SBA-16, respectively.

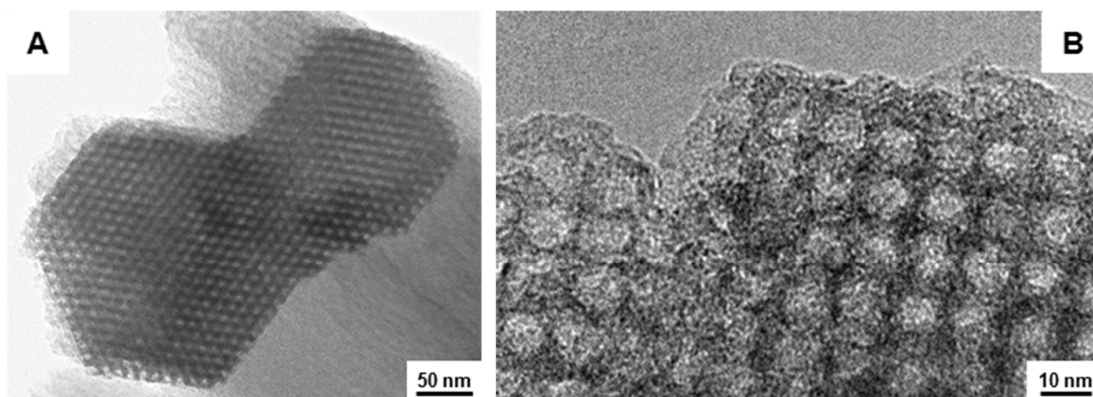


Figure 1. TEM images of mesoporous supports, (A) SBA-15 and (B) SBA-16.

SBA-15 fibers and rods were obtained by performing the ripening process under agitation or quiescent conditions, respectively. The elongated shape is originated by the micelles alignment due to the shear force produced by the stirring [34]. Table 1 presents the main morphology of particles and the textural properties. S15/F is composed of aggregates of fibers cross-linked with a length around 30-40 μm and thickness of 5 μm ; while S15/R material presented mainly short rod-shaped particles, which have a length of up to 1 μm and thicknesses around 200 nm.

Regarding SBA-16, the combination of high acidity and temperatures can lead to spherical particles by different mechanisms [35]. S16/S exhibited the spherical morphology with homogeneous diameters, which varies between 2 and 5 μm .

On the other hand, the shapeless particles observed on SBA-16 (S16/I) with a wide range of sizes, between 2 and 30 μm , is related to TEOS concentration and use of butanol [36]. The

butanol (co-surfactant) allows to obtain the cubic mesophase in a wider range of precursors concentration.

Table 1. Morphology and textural properties of silica mesoporous supports.

Supports	Morphology	S_{BET} (m² g⁻¹)	Vp^a (cm³ g⁻¹)	Dp^b (nm)
S15/F	Fibers	650	0.70	8.2
S15/R	Rods	570	0.70	6.7
S16/S	Spheres	680	0.53	6.0
S16/I	Irregular	650	0.45	6.2

^a Total pore volume at $P/P^0 = 0.97$

^b Maximum in the pore size distribution from BJH-KJS method

N₂ physisorption isotherms of the supports were measured in order to obtain information about the mesoporosity and textural properties. The isotherms are characterized by a typical IUPAC type IVa, with hysteresis loops, which is distinctive for mesoporous materials [37]. S15/F exhibited a H1 hysteresis cycle and a pore size distribution centered at 8.2 nm (calculated by the BJH-KJS method). On the other hand, S15/R presented a relatively narrow pore size distribution with the maximum at 6.7 nm. Both materials would reveal the presence of uniform cylindrical mesopores (Figure S1, Supplementary material). Furthermore, S15/F and S15/R showed specific area typical values of SBA-15 materials, 650 and 570 m² g⁻¹ respectively, and pore volume of 0.7 cm³ g⁻¹ for both supports (Table 1).

Loop hysteresis of H2 type, correlated with the presence of “ink-bottle” type mesoporous is found for SBA-16 solids. In this vein, the isotherms presented adsorption branches depicting gradual pore filling. In the desorption branches, the pore emptying process occurs when an abrupt decrease in N₂ adsorbed volume is observed, located at P/P^0 around 0.42 (critical value for N₂ at 77 K). The pore size distribution profiles exhibited maxima centered at 6.0

and 6.2 nm, for S16/S and S16/I, respectively (Figure S1). It is noteworthy that the closing points of hysteresis loops of isotherms (desorption branch) would indicate that the pore windows are around 4 nm or smaller [37]. In addition, for these materials the specific surface areas were 680 and 650 m² g⁻¹ (Table 1).

3.2 Influence of oxides concentration. COPrOx

In order to analyze the effect of the concentration of CuO and CeO₂ active oxides on catalytic reaction, SBA-15 fibers support (S15/F) was chosen for its uniform morphology and better textural properties. Table 2 shows three formulations of catalysts obtained by incipient wetness impregnation method, where the relative concentrations of CuO, defined as the mass ratio CuO/(CuO + CeO₂), were 0.15, 0.20 and 0.50.

The textural properties analysis revealed a decrease in surface area and pore volume in comparison with the as-synthesized material, which is related to the incorporation of the oxide nanoparticles inside the mesostructures. It is interesting to note that S15/F-0.20 showed the highest values (S_{BET} and V_p) although it did not have the lowest active phase loading. While this material presented a surface area loss around 35 %, S15/F-0.15 and S15/F-0.50 displayed values near 50 % (Table 2).

Table 2. Composition, textural properties and catalytic data of similar catalysts in the literature.

Catalysts	CuO-CeO ₂ (wt. %)	S _{BET} (m ² g ⁻¹)	V _p ^b (cm ³ g ⁻¹)	D _p ^c (nm)	W/F (g s mL ⁻¹)	T max. conv. (°C)	References
S15/F-0.15 ^a	4.4-24.3	335	0.42	8.0	0.14	175	Present work
S15/F-0.20 ^a	4.8-18.9	430	0.52	7.5	0.14	175	Present work
S15/F-0.50 ^a	10.0-9.8	313	0.45	7.7	0.14	210	Present work
5CuCe/SBA-15- SSI	5.0-20.0	540	0.62	7.5 ^d	0.20	120	[30]
Si-6Cu20Ce	7.5-24.5	328	0.48	n.r.	0.18	115	[38]
SBACe20Cu6	7.5-24.5	139	0.16	3.8 ^d	0.18	140	[29]

^a Mass relative CuO concentration

^b Total pore volume at $P/P^0 = 0.97$

^c Maximum in the pore size distribution from BJH-KJS method

^d Pore size distribution from BJH method

All studied catalysts presented typical curves of CO and O₂ conversions, where the CO conversion increased as the reaction temperature increased (Figure S2). After a maximum value, CO conversion decreased by the occurrence of the undesired H₂ oxidation reaction, more thermodynamically favorable at high temperatures.

Figure 2 (3-D image, orthographic projection) shows the maximum CO conversion achieved and CuO and CeO₂ oxide concentrations for our catalysts (with different relative CuO concentration) and values reported by other researchers [29,30,38]. It is clear that an increase in the relative CuO concentration did not lead to a better catalytic behavior, since there was an optimal value within the range studied. The S15/F-0.20 material was the most active catalyst, with more than 99 % CO conversion at 175 °C, while S15/F-0.15 achieved 74 % at the same temperature. On the other hand, the catalyst prepared with a relative concentration of CuO equal to 0.5 (S15/F-0.50) was less active, reaching CO conversion slightly higher than 30 % at 210 °C. The O₂ selectivity values towards CO₂ decreased as the temperature

increased. In the best catalyst, the selectivity value resulted above 80 % up to 150 °C; in the maximum CO conversion, the selectivity was around 50-60 % (Figure S2).

In the state of the art, there are only a few papers where the active phase CuO-CeO₂ was dispersed in different supports and evaluated for COPrOx reaction. For this reason, and the diverse reaction conditions selected, a direct performance comparison is very complex. It should be kept in mind that the main objective of COPrOx catalysts is to maximize CO conversion at the lowest temperature possible. Catalytic behavior of the previous works generally presented an optimal copper concentration, without an improvement in activity for higher amount of copper. In particular, our catalyst S15/F-0.20 showed a CO conversion window above 90 % between 150 and 190 °C (Figure S2). Tang and coworkers [30] reported CuO-CeO₂/SBA-15 catalysts synthesized with different compositions by solid state impregnation and wet impregnation. The best material, with CuO 5 wt. % (Table 2 and Figure 2, green bar) presented more than 99 % CO conversion between 120 and 180 °C. This composition led to remarkable increase in catalytic activity against the values of 1 and 3 wt. %, while a load of 10 wt. % did not result in corresponding enhancement in the activity. Cecilia et al. [38] studied different copper loadings in CuO-CeO₂ based catalysts supported on porous clay. The sample with 6 wt. % of copper displayed CO conversion value close to 100 % at 115 °C (Table 2 and Figure 2, red bar). Furthermore, Reyes Carmona et al. [29] also reported an optimal loading of Ce and Cu supported on SBA-15 mesoporous silica doped with Zr, whose compositions are close to the best catalysts previously mentioned. Additionally, they found that the incorporation of Zr into the support increased the conversion of CO and the selectivity to CO₂ in comparison with the sample without Zr, which presented a conversion of 95 % at 140 °C (SBACe20Cu6, Table 2 and Figure 2, pink bar).

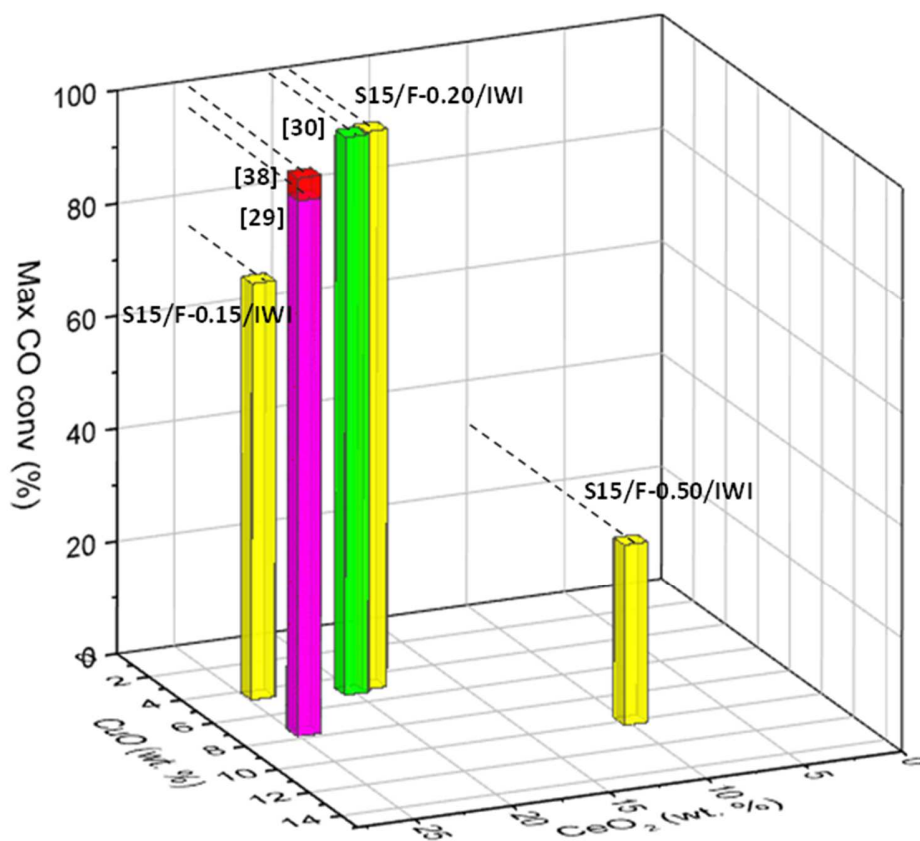


Figure 2. Maximum CO conversion and CuO and CeO₂ concentrations of catalysts supported on SBA-15. This work (yellow bars) and references [29] pink bar, [30] green bar and [38] red bar.

Other studies based on Cu-Ce bulk catalysts analyzed the variation in the composition of the synthesized materials and its possible influence on COPrOx. Gu et al. [39] prepared highly ordered mesoporous Cu-Ce-O catalysts with different copper content (5-70 mol %), where Cu_{0.2}Ce_{0.8}O₂ showed the best results (CO conversion around 100 %). Guo and coworkers [18] obtained a series of CuO/CeO₂(rod) catalysts with varying copper loadings and analyzed the effect of increase of Cu coverage on the surface of CeO₂ particles. They also found an

optimal percentage above which the CuO particles dispersion was reduced, the interfacial Cu-Ce interaction was weakened and their CO conversion declined. Jampa et al. [17] evaluated CuO/mesoporous ceria catalysts prepared by deposition-precipitation with different loadings of Cu (3, 5, 7 and 9 wt. %) on COPrOx. The catalysts showed 100 % conversion at 130 °C, but the CuO 7 % concentration material had the highest reaction rate (at temperatures below the maximum conversion temperature).

3.3 Influence of incorporation method and precursors. COPrOx

Incipient wetness impregnation (IWI) and solid state impregnation (SSI) were selected to analyze a possible influence of the oxides incorporation method on catalytic behavior. For this purpose, two catalysts based in the best formulation (S15/F-0.20, according to the previous study), were prepared by both techniques. In addition, alternative copper and cerium precursors (acetates instead of nitrates) were used in an IWI preparation (IWI*). Figure 3 represents the catalytic behavior of the mentioned materials and a reference bulk catalyst (CuO-CeO₂) at the temperature of maximum CO conversion. From the graph, it can be noticed that both catalysts prepared by incipient wetness impregnation with nitrates (IWI) or acetates (IWI*) showed similar conversions and selectivity values. The catalysts reached more than 99 % of CO conversion at the same temperature (175 °C). Regarding selectivity and oxygen consumption values were very close as well; however, the IWI catalyst was slightly better. Taking into account the synthesis stages, in the first step, the nitrate or acetate precursors were dissolved in a liquid medium (ethanol); then, in contact with the mesoporous support the ions diffused into the cavities of the solid. In a second stage, the ethanol was evaporated during the drying step and finally the precursor anions (acetates or nitrates) were

completely decomposed in the air flow at 450 °C. CuO and CeO₂ dispersed nanoparticles were formed inside the pores. Although other authors have found differences in the use of different Cu precursors to synthesize CuO-CeO₂ bulk catalysts [40], in our catalysts it seems that these differences become negligible when the active phase is introduced in the mesostructure.

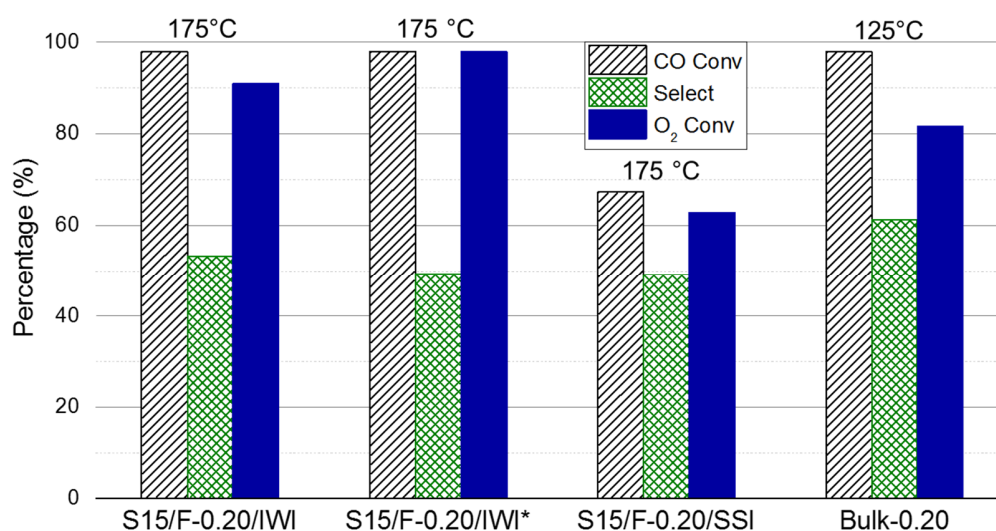


Figure 3. CO conversion, O₂ conversion and selectivity to CO₂ at maximum CO conversion temperature of CuO-CeO₂ catalysts based on S15/F. Reaction conditions: 1% CO, 1% O₂, 40% H₂ in He balance; $\tau = 0.138 \text{ g}_{\text{cat}} \text{ s mL}^{-1} \text{ STP}$.

On the other hand, if S15/F-0.20/IWI and S15/F-0.20/SSI are compared, it can be observed that both showed their maximum CO conversion at the same temperature (175 °C); however, the material prepared by solid state impregnation presented significantly less CO and O₂ conversions. These observations suggest that the solid state impregnation is not as effective as the incipient wetness impregnation to ensure an intimate contact between CuO and CeO₂

phases. SEM images and EDS analyses (Figure S3) revealed a more homogenous distribution of copper and cerium for S15/F-0.20/IWI compared to S15/F-0.20/SSI. The EDS data obtained for different points on the solid particles showed that molar concentration of Cu, Ce and Si was very close to the nominal values for catalyst prepared by IWI method. While the SSI method produced particles with a certain degree of heterogeneity. The homogeneous distribution obtained by IWI method favors the interaction between copper and cerium species, promoting the catalytic activity.

Finally, the bulk catalyst prepared by coprecipitation (Bulk-0.20) showed CO conversion above 99 % and 60 % selectivity of CO to CO₂ at lower temperature (125 °C) than other catalysts. Similar results were published by other authors for CuO-CeO₂ catalysts [18,30,41]. It should be noted that the mass of catalyst used for the catalytic test was the same (0.2 g), therefore Bulk-0.20 contains more than four times the amount of CuO and CeO₂ oxides than the catalysts based on mesoporous silica. On the other hand, XRD analysis of Bulk-0.20 showed that no signals of copper species were visible suggesting that no big clusters of CuO are present (Figure S4). Then, its better catalytic behavior could be attributed to its higher amount of oxides and their intimate contact promoted by the lack of a silica support.

It is important to mention that the CO oxidation reaction over copper-cerium systems follows a reaction pathway known as the Mars van Krevelen mechanism. In this mechanism a series of steps are involved; first, CO molecules are chemisorbed over Cu ions active sites (Cu⁺) and therefore activated generating Cu⁺-CO species. Then, Cu⁺-CO species react with nearby active oxygen (lattice oxygen provided by CeO₂) over Cu-Ce oxides and CO₂ is formed. As a final step, the oxygen vacancy produced is refilled by gas phase oxygen incorporated in the reaction. It is apparent that the proximity of the Cu⁺ species with ceria is key, specifically the

interface where the significant active centers allow the advance of the CO oxidation process. Therefore, a support could modify the synergistic interaction between Cu and Ce oxides compared with that existing in the bulk system and influencing in catalytic performance.

3.4 Influence of support structure. COPrOx

Due to its satisfactory catalytic results and simplicity of preparation, the incorporation of the nitrates by incipient wetness impregnation was selected for further experiments.

Figure 4 presents the catalytic values at maximum CO conversion of formulations with differences in the morphology and mesostructure of the used supports. In addition, the complete curves of catalytic performance are shown in Figure S2.

As mentioned before, for the synthesis of the SBA-15 silicas, changes in agitation at the ripening stage were introduced in order to obtain materials in the shape of fibers or rods. Similarly, modifications in the physical and chemical factors of the synthesis of SBA-16 were made, obtaining sphere or irregular-shaped particles.

The top section of the Figure 4 exhibits the SEM images of the corresponding catalysts prepared from the previously described silicas. The micrographs revealed that the size of the fibers was reduced from 30-40 μm (length) to 10-20 μm after the incorporation of the copper and ceria species. In contrast, no changes in shape or size in the other materials were detected. This suggests that the IWI technique introduces mechanical stress during the mixing step, causing segregation and breakage of the fibers. However, the other geometries, with smaller aspect ratios, are presumably more resistant and result less damaged. In addition, the micrograph of S16/S-0.20/IWI revealed the presence of brighter spots in the surface of the

spheres, probably ascribable to the incomplete incorporation of the active oxides inside the mesopores.

From the bar graphic (Figure 4), it can be observed that the both SBA-15 based catalysts presented the highest CO conversion, being the fiber morphology the most active and selective formulation. In the case of S15/R-0.20/IWI, it exhibited its maximum conversion of 84 % at 175 °C.

Among the SBA-16 based catalysts, the irregular shaped material showed the better performance with a CO conversion of 80 % at 175 °C. Regarding S16/S-0.20/IWI it reached its maximum CO conversion (64 %) at 200 °C showing maximum oxygen consumption and poor selectivity.

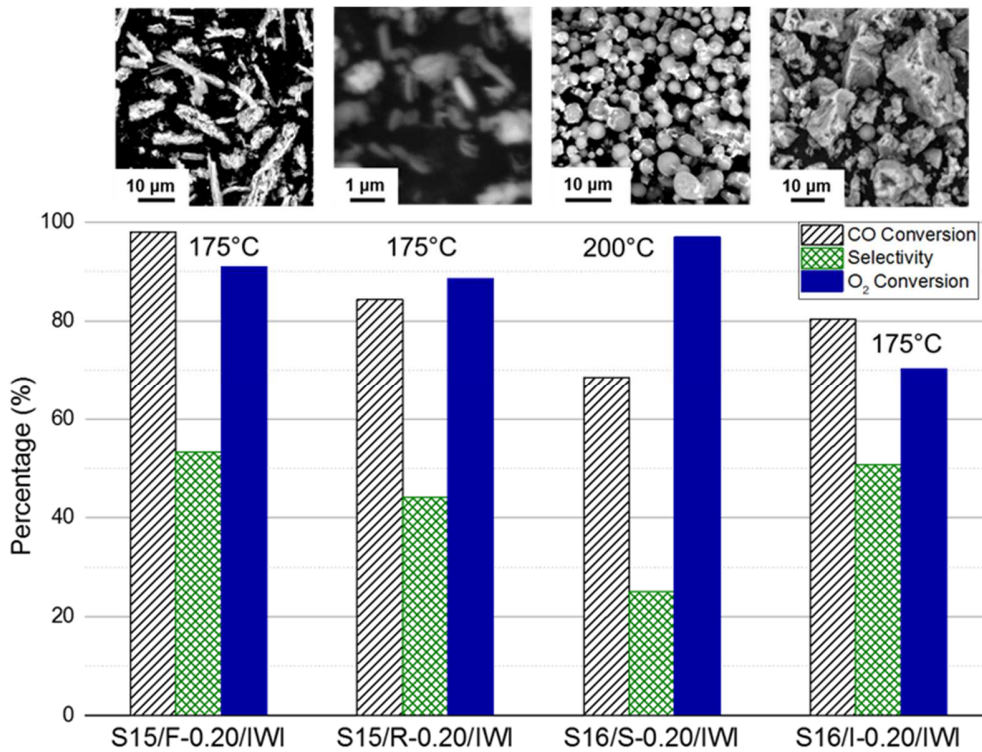


Figure 4. CO conversion, O₂ conversion and selectivity to CO₂ at maximum CO conversion temperature of catalysts obtained by IWI method; at the top, corresponding SEM images. Reaction conditions: 1% CO, 1% O₂, 40% H₂ in He balance; $\tau = 0.138 \text{ g}_{\text{cat}} \text{ s mL}^{-1} \text{ STP}$.

From these results, it can be concluded that the 2-D structure of the SBA-15 results more suitable than SBA-16 for this application, probably due to its wider pores with uniform diameter, favoring the contact between the reagents and the active phase. Similar results were observed by Szegedi and co-workers [42] where they attributed the lower catalytic activity of SBA-16 supported materials to the hindering effect of its characteristic pore structure, limiting the penetration of the precursor salts.

3.5 Long-term reaction and influence of inhibitors. COPrOx

In addition, the effect of CO₂ and H₂O over the S15/F-0.20/IWI catalyst was studied under reaction conditions at 175 °C. The results are exhibited in Figure 5. At the beginning of the reaction, the catalyst is absence of inhibitors (left white region of the graph). When 10 % CO₂ was added to the feed (yellow section), a decrease of conversion and selectivity values was observed and they stabilized around 90 % and 48 % respectively, these values remained fairly constant for 42 h. Subsequently, both 10 % H₂O and 10 % CO₂ were simultaneously added (highlighted in pink) to the reactor.

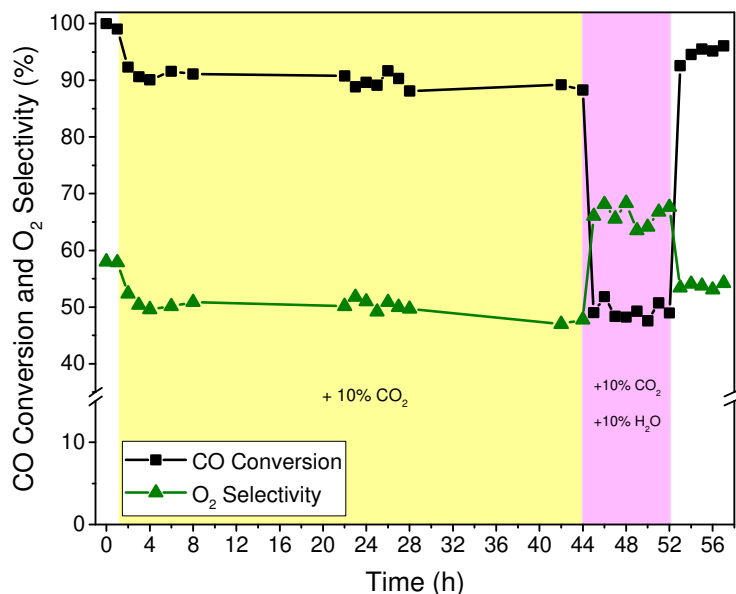


Figure 5. Effect of CO₂ and H₂O on COPrOx for S15/F-0.20/IWI at 175 °C in long-term reaction. Reaction conditions: 1% CO, 1% O₂, 40% H₂, 10% CO₂ and 10% H₂O, in He balance; $\tau = 0.138 \text{ g}_{\text{cat}} \text{ s mL}^{-1} \text{ STP}$.

Under these conditions, a further decrease in the conversion (up to 50 %) was observed as well as a significant increment in the selectivity (reaching 68 %), which remained constant for 8h. Former studies [17,43,44] have observed similar behaviors in CuO-CeO₂ systems in the presence of water and carbon dioxide. In this vein, the adsorption of CO₂ competes with CO for the active sites decreasing the CO conversion. On the other hand, the water in the feed has a blocking effect since it not only further inhibits the CO oxidation, but also strongly affects the reaction between H₂ and O₂, evidenced by the increase in selectivity in the pink region of Figure 5.

In the last step of the experiment, CO₂ and H₂O were withdrawn and the system returned to the original reaction conditions. At this stage, it could be observed that the conversion and

selectivity values were close to those obtained at the beginning of the experiment (white regions). The recovery of activity and selectivity suggests that the adsorbed surface species were removed by either desorption or decomposition mechanisms.

3.6 Catalysts characterization

Figure 6 shows TEM images of catalysts prepared by IWI method on different SBA-15 and SBA-16 morphologies. In the two mesostructures, the porous arrangement was clearly conserved. Also, the oxides nanoparticles were homogeneously incorporated in the channels or pores. Regarding to the copper and cerium oxides particle sizes, distributions were estimated from these images and are shown inset in Figure 6. All materials presented an average size of active phase smaller than 10 nm. Micrographs of SBA-15 based catalysts presented CuO-CeO₂ nanoparticles with an elongated-shaped within parallel channels, and an average size around 7.7 nm. Probably, this morphology generated a greater dispersion in the distribution as suggested by standard deviations. On the other hand, the nanoparticles incorporated in SBA-16 presented more homogeneous size, between 5.7 and 6.5 nm, with apparently more spherical shapes. The porous structure could constrain the shape and size of the nanoparticles, inside spherical cavities in SBA-16 and cylindrical channels in SBA-15. In addition, the particles are slightly larger within the porosity of SBA-15 compared to SBA-16.

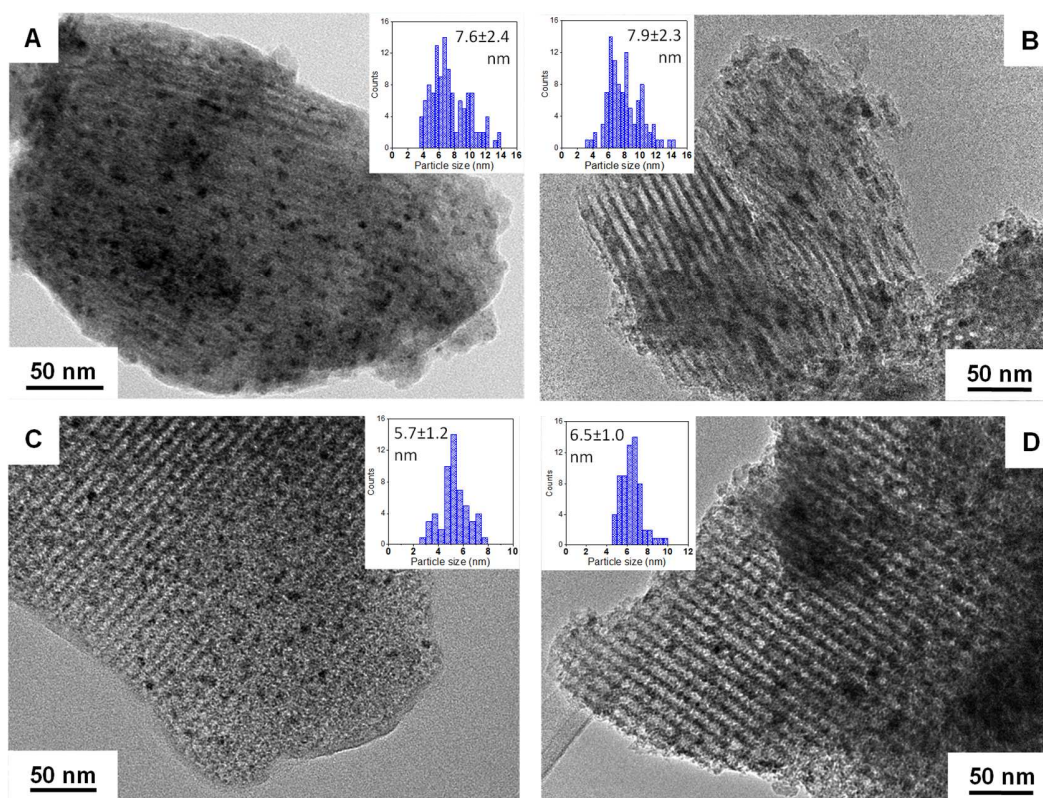


Figure 6. TEM images and particle size distribution of (A) S15/F-0.20/IWI, (B) S15/R-0.20/IWI, (C) S16/S-0.20/IWI and (D) S16/I-0.20/IWI catalysts.

STEM images corresponding to S15/F-0.20/IWI and S16/I-0.20/IWI are shown in Figure 7. As noted by TEM analysis, in both materials the oxides nanoparticles incorporated by IWI method as well as the mesoporous structure preservation were observed. Small bright spots homogeneously distributed were found in the images, which correspond to the active phase nanoparticles. Furthermore, the EDS spectra of the images allowed to verify the presence of copper and cerium species and the silicon of supports. The size of the nanoparticles and the homogeneous distribution of active oxides inside the cavities promote a strong interaction between CuO and CeO₂ in these materials.

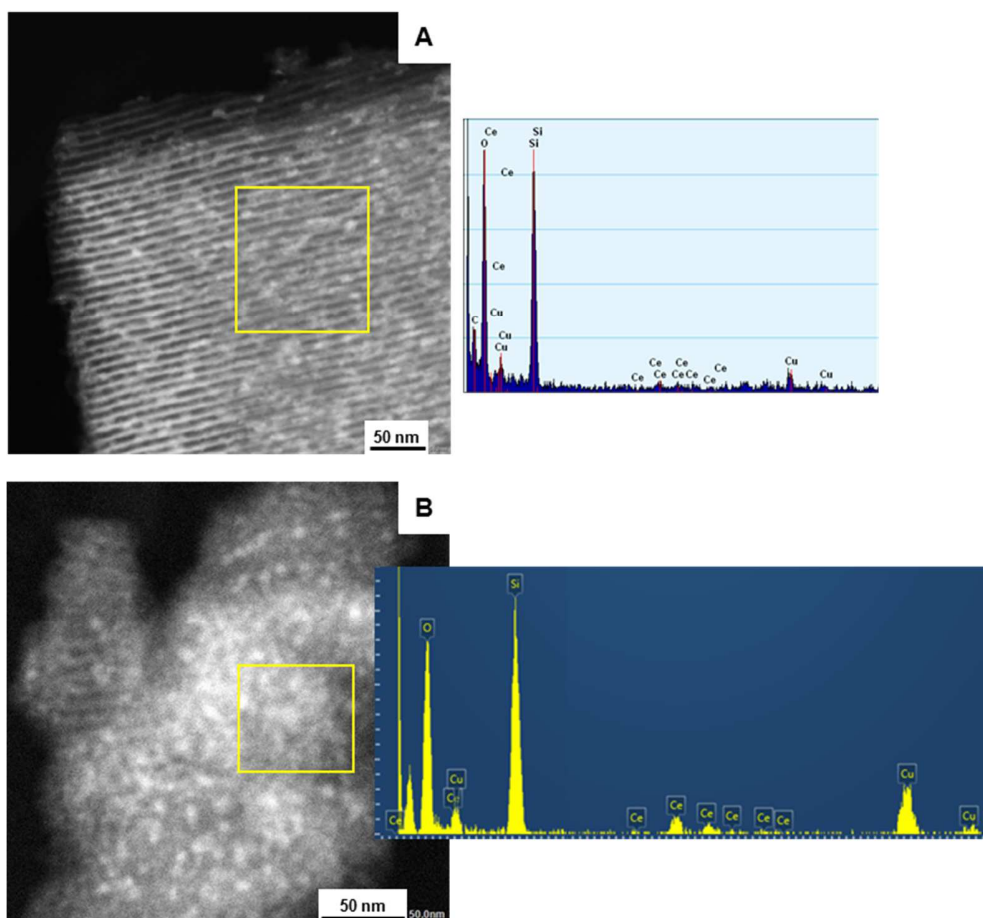


Figure 7. HADDF-STEM images and EDS spectrum of area selected of (A) S15/F-0.20/IWI, (B) S16/I-0.20/IWI catalysts.

X-ray diffraction technique (wide-angle) was applied for the catalysts based on SBA-15 fibers (Figure S4). For comparison, Bulk-0.20 and S15/F-Ce diffractograms were also analyzed. The ceria pattern was detected in all materials, with characteristic signals of fluorite phase. The main peaks at 2 theta 28.58, 33.11, 47.52, 56.38° (JCPDS N° 34-0394) and a broad signal around 25° (approx. between 17 and 30°) corresponding to amorphous silica were observed. Concerning the signals of copper species, they were not detected in any catalysts, probably their sizes were below the detection limit of the diffractometer. The ceria

lattice parameter values of all catalysts are smaller than the monometallic reference S15/F-Ce (Table S1). These results would suggest the incorporation of a fraction of Cu species into the ceria lattice, since smaller Cu^{2+} ions (0.73 Å) can be hosted by the ceria lattice (Ce^{4+} , 0.97 Å). In particular, similar values of this parameter in the catalysts with relative CuO concentration of 0.20 prepared from the different precursor salts can be observed. Furthermore, the average ceria crystallite size of five catalysts (calculated by Scherrer's equation, Table S1) was between 4.5 and 5.6 nm, in agreement with TEM observations.

XPS technique was used to characterize the chemical state and surface composition of ceria-based catalysts, the results are presented in Table 3. The nominal Cu/Si and Ce/Si are 0.047-0.121, 0.047-0.085 and 0.094-0.043 for 0.15, 0.20 and 0.50 formulations, respectively. It is found that, with the exception of S16/S-0.20/IWI, all the catalysts have smaller Cu/Si and Ce/Si surface ratios than the nominal ones. The reason behind this phenomenon is the low penetration of the X-ray beam and shielding effect of the silica structure. Regarding the Cu and Ce surface enrichment observed in the sphere based catalyst, it is consistent with the presence of catalyst in the outer surface of the spheres as previously described. The Cu/Ce surface molar ratios were in general close to the nominal values (0.39, 0.55 and 2.2 for 0.15, 0.20 and 0.50 relative CuO concentrations, respectively).

The Cu 2p spectra present a main peak above 933.8 eV and a shake-up satellite between 938.0-948.0 eV which are characteristic of CuO and therefore, evidence the existence of Cu^{2+} in all the studied materials. In addition, reduced Cu species were found, sustained by an asymmetry in the main peak at lower binding energies values (932.9-933.2 eV). For estimating the amount of reduced copper species, the intensity ratio between the satellite and main peaks was calculated. According to this method, a result of 0.55 indicates that all the

copper is in its 2+ state, and 0 indicates that all the copper is reduced (Cu^+ or Cu^0). From the $I_{\text{sat}}/I_{\text{mp}}$ values presented in Table 3, it can be observed that apart from S15/F-0.50/IWI and S16/S-0.20/IWI, all materials exhibited values lower than 0.55 suggesting the presence of partially reduced surface copper species in those catalysts.

In this vein, numerous authors have proposed that the presence of reduced surface copper species is related to the intimate interaction between CuO and CeO₂ oxides because of the existence of the redox balance ($\text{Ce}^{3+} + \text{Cu}^{2+} \leftrightarrow \text{Ce}^{4+} + \text{Cu}^+$) [22]. This appears evident when the low COPrOx performance exhibited by S15/F-0.50/IWI and S16/S-0.20/IWI are considered, since Cu^+ is regarded as an adsorption site for CO in COPrOx reaction [45].

Table 3. XPS data of selected catalysts.

Catalysts	$I_{u''}/I_{\text{Ce tot}}^a$	$I_{\text{sat}}/I_{\text{mp}}^b$	Surface atomic ratios ^c		
			Cu/Ce	Cu/Si	Ce/Si
S15/F-0.15/IWI	0.14	0.37	0.50	0.03	0.05
S15/F-0.20/IWI	0.13	0.25	0.63	0.02	0.03
S15/F-0.50/IWI	0.13	0.55	2.87	0.07	0.02
S15/F-0.20/SSI	0.14	0.26	0.82	0.03	0.04
S15/R-0.20/IWI	0.14	0.38	0.55	0.02	0.03
S16/S-0.20/IWI	0.14	0.55	0.30	0.28	0.93
S16/I-0.20/IWI	0.12	0.33	0.65	0.02	0.03

^a The intensity ratio between u'' peak and the total contribution of Ce 3d

^b The intensity ratio between Cu 2p 3/2 satellite peak and the principal peak

^c Surface atomic ratio, calculated considering Cu 2p_{3/2}, Ce 3d_{5/2} and Si 2p regions

Figure 8 displays the Cu 2p_{3/2} spectra of S15/F-0.15/IWI, S15/F-0.20/IWI and S15/F-0.50/IWI. As shown in the figure, a third signal centered at 935.6 eV was found in the catalyst with the highest amount of copper (S15/F-0.50/IWI). This signal at higher binding energy is attributed to copper species in strong interaction with the support $\text{Cu}^{2+}\text{-O-Si}$, where a charge

transfer from the metal ion toward the silica matrix occurs [46]. This conduces to a decrease in catalytic activity, since a fraction of copper species do not interact with CeO₂.

Regarding the Ce 3d spectra, Ce⁴⁺ was found in all catalysts. The CeO₂ spectrum consists in several peaks, for each component of spin orbit split doublet (usually labelled as v and u) contains three peaks. In the higher binding energy region: u (900.8-901.3), u'' (907.6-908.5) and u''' (916.9-917.2) can be found, and they are associated to the Ce 3d_{5/2} spectra. At lower binding energies: v (882.6-883.6), v'' (889.0-889.6) and v''' (898.5-898.9) peaks are assigned to Ce 3d_{3/2}. The presence of Ce³⁺ can be detected by two extra signals: v' at 884.1-885.1 eV belong to Ce 3d_{5/2}, and u' at 903.1-903.4 eV correspond to Ce 3d_{3/2}.

The method described by Larachi et al. [47] was used to determine the reduction degree of cerium, where the intensity of the u''' peak is calculated over the intensity total spectrum. This method is based on the fact that the signal u''' located around 917.0 eV does not overlap with the other seven components mentioned above. In this way, due to the absence of u''', the I_{u'''}/I_{Ce tot} ratio is equal to 0 when all the cerium is in its oxidation state (3+) and is equal to 0.14 when all cerium is found as CeO₂ (Ce⁴⁺). According to the I_{u'''}/I_{Ce tot} values displayed in Table 3 show that the cerium species present in the catalysts surface are mainly in their as Ce⁴⁺. A ratio below 0.14 can be found in some samples indicating that Ce³⁺ and Ce⁴⁺ species are simultaneously presented, which can be associated to oxygen vacancies and due to the small particle size of ceria particles.

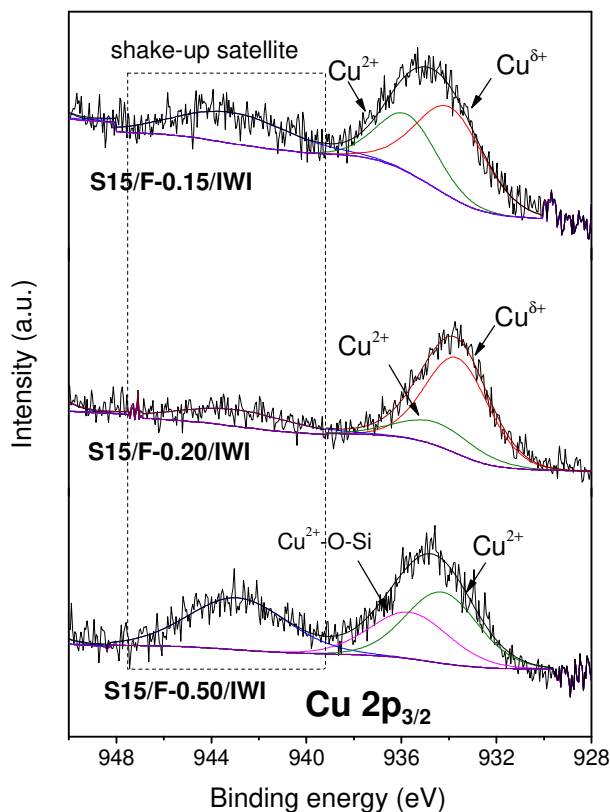


Figure 8. XPS spectra of S15/F-0.15/IWI, S15/F-0.20/IWI and S15/F-0.50/IWI catalysts.

4. Summary

Regarding the synthesis of SBA-15, by changing the ripening stage conditions (with or without stirring) it is possible to obtain long fibers or short rods, where the S_{BET} and D_p were slightly lower in the latter. In comparison, the SBA-16 materials showed similar specific surface area and lower V_p and D_p . In general, the high surface area of the supports benefited the dispersion of CuO and CeO₂ oxides nanoparticles. In addition, the catalysts displayed the preservation of the mesostructure and the formation of nanoparticles of active phases (less than 10 nm) detected by TEM in agreement with XRD results.

According to the presented data it can be concluded that Cu and Ce loadings are important variables to take into account when developing CuO-CeO₂ catalysts and especially, supported catalysts. From the catalytic results it is observed that the best relative CuO concentration was 0.2 where the conversion of CO is above 90 % in a wide window of temperatures. In this sense, ourselves and other authors have found that increasing in the relative concentration of copper is beneficial up to a certain point (Figure 2). After that value, subsequent increases in the copper load worsen the catalytic performance of the materials. This behavior suggests, that if the amount of ceria is enough, an increase in copper loading conduces to the formation of more CuO-CeO₂ active sites. However, an excessive quantity of copper can lead to CuO particles with no or weak interaction with ceria, and strong interaction with the silica support instead (as evidenced by XPS spectra).

Regarding the use of alternative precursors, it seems that the insertion of the active phase within the mesopores damped the possible differences in the catalytic activity. This could be ascribed to the fact that, as long as there is good contact between copper and cerium species, the constraining effect of mesostructure can control the particle size and homogenize the differences. In this sense, the IWI method offers the advantage of being simple and straightforward to achieve a highly dispersed active phase. In contrast, the use of the same precursors incorporated by SSI technique conducted to a significantly less CO conversion, which could be related to less interaction between copper and cerium species or to the enrichment in surface copper, as indicates the Cu/Ce ratio calculated from XPS data.

The mesostructure also had a marked effect in the catalytic behavior. The better performance of SBA-15 based material is associated to its wider and uniform pores. In this vein, the “ink-bottle” pores with windows of 4 nm or smaller can easily be blocked by the active species

deposited, preventing access of reagents to a portion of the active sites. This hypothesis is sustained by the average size of nanoparticles measured by TEM which were close to the maximum diameter of the main pores and bigger than 4 nm. In particular, the low activity of S16/S-0.20/IWI may be a consequence of the accumulation of active phase on the surface of the spheres detected by SEM, with a poor distribution of oxides in the mesoporous cavities. Moreover, this catalyst exhibited no signs of reduced copper species in its surface, which contributed to its low CO conversion value.

The decrease of ceria lattice parameter values observed in presence of copper suggested the partial incorporation of Cu species into the ceria network. Moreover, the analysis of the nature of the chemical species carried out by XPS revealed that in fresh catalysts the majority species were Ce^{4+} . However, in the most active catalyst, species of Ce^{3+} are also present, which are associated with vacancies oxygen and favor the redox process. Likewise, in the Cu 2p spectra (Figure 8), two components appear, one corresponding to Cu^{2+} and the other with a lower binding energy associated with Cu^+ species recognized as a key site of CO adsorption in the reaction mechanism. In addition, in the sample with the highest $\text{CuO}/(\text{CuO}+\text{CeO}_2)$ ratio, copper species strongly linked to the silica support ($\text{Cu}^{2+}\text{-O-Si}$) were found.

The relative surface concentrations Cu/Si and Ce/Si calculated from the XPS data, were lower than the nominal values, which confirms the high dispersion of the copper and cerium species inside the cavities. Conversely, for the catalyst prepared from SBA-16 in the form of spheres, a higher surface concentration of copper and cerium was observed, in agreement with the SEM observations.

Although the time on stream experiment results returned expected catalytic behavior under the different feed conditions, it is noteworthy that the slight decrease in CO conversion can

be related to the confining effect of the mesostructure, preventing sintering by migration of the active species and consequent loss of active sites.

5. Conclusions

In this study, an optimal relative CuO concentration value which maximizes the CO conversion in CuO-CeO₂ catalysts supported on mesoporous silicas was found.

By selecting synthesis parameters such as agitation, directing agents, co-surfactants, temperatures and acidity, among others, SBA-15 (fibers or rods) and SBA-16 (spheres or shapeless particles) were obtained. The catalysts prepared from these materials preserved their mesostructure with a homogeneous distribution of CuO-CeO₂ nanoparticles (< 10 nm) inside the pores.

The incipient wetness impregnation method was the better alternative to introduce the active oxides compared to solid state impregnation. In addition, the catalysts based on 2-D structure of SBA-15 were more active and selective than the based in 3-D SBA-16.

The best COPrOx catalyst S15/F-0.20/IWI, obtained from the SBA-15 fibers with a relative CuO concentration of 0.2, exhibited $X_{CO} \geq 99 \%$ at 175 °C. It was also evaluated for several hours with addition of carbon dioxide and water and showed an adequate performance and good recovery of CO conversion and selectivity.

Acknowledgments

The authors wish to acknowledge the financial support received from UNL, ANPCyT, and CONICET and to Ministry of Science, Technology and Innovation of Santa Fe (MinCTIP-

ASACTei) for the Grant (AC-2015-0002) for the purchase of TEM -JEOL 2100-plus. Thanks are given to María Fernanda Mori (INCAPE, Santa Fe, Argentina) for the XPS measurements and to Ludovic Josien (IS2M, Mulhouse, France) for SEM-EDS analyses.

References

- [1] K. Azad, M. Rasul, eds., *Advanced Biofuels. Applications, Technologies and Environmental Sustainability*, first ed., Woodhead Publishing, Cambridge, 2019. doi:<https://doi.org/10.1016/C2018-0-00461-2>.
- [2] M.S. Javed, T. Ma, J. Jurasz, M.Y. Amin, Solar and wind power generation systems with pumped hydro storage: Review and future perspectives, *Renew. Energy*. 148 (2020) 176–192. doi:[10.1016/j.renene.2019.11.157](https://doi.org/10.1016/j.renene.2019.11.157).
- [3] H. Nazir, C. Louis, S. Jose, J. Prakash, N. Muthuswamy, M.E.M. Buan, C. Flox, S. Chavan, X. Shi, P. Kauranen, T. Kallio, G. Maia, K. Tammeveski, N. Lymperopoulos, E. Carcadea, E. Veziroglu, A. Iranzo, A.M. Kannan, Is the H₂ economy realizable in the foreseeable future? Part I: H₂ production methods, *Int. J. Hydrogen Energy*. 45 (2020) 13777–13788. doi:[10.1016/j.ijhydene.2020.03.092](https://doi.org/10.1016/j.ijhydene.2020.03.092).
- [4] F. Xie, Z. Shao, M. Hou, H. Yu, W. Song, S. Sun, Recent progresses in H₂-PEMFC at DICP, *J. Energy Chem*. 36 (2019) 129–140. doi:[10.1016/j.jechem.2019.07.012](https://doi.org/10.1016/j.jechem.2019.07.012).
- [5] P. Jing, X. Gong, B. Liu, J. Zhang, Recent advances in synergistic effect promoted catalysts for preferential oxidation of carbon monoxide, *Catal. Sci. Technol*. 10 (2020) 919–934. doi:[10.1039/C9CY02073J](https://doi.org/10.1039/C9CY02073J).
- [6] Y. Chen, J. Lin, L. Li, X. Pan, X. Wang, T. Zhang, *Applied Catalysis B*:

- Environmental Local structure of Pt species dictates remarkable performance on Pt/Al₂O₃ for preferential oxidation of CO in H₂, *Appl. Catal. B Environ.* 282 (2021) 119588. doi:10.1016/j.apcatb.2020.119588.
- [7] D.I. Potemkin, E.Y. Filatov, A. V Zadesenets, A.M. Gorlova, N.A. Nikitina, D.A. Pichugina, A comparative study of CO preferential oxidation over Pt and Pt_{0.5}Co_{0.5} nanoparticles: Kinetic study and quantum-chemical calculations, *Mater. Lett.* 260 (2020) 126915. doi:10.1016/j.matlet.2019.126915.
- [8] R. Castillo, E. Dominguez Garcia, J.L. Santos, M.A. Centeno, F. Romero Sarria, M. Daturi, J.A. Odriozola, Upgrading the PtCu intermetallic compounds: The role of Pt and Cu in the alloy, *Catal. Today.* 356 (2020) 390–398. doi:10.1016/j.cattod.2019.11.026.
- [9] L.E. Gómez, B.M. Sollier, A.M. Lacoste, E.E. Miró, A.V. Boix, Hydrogen purification for fuel cells through CO preferential oxidation using PtCu/Al₂O₃ structured catalysts, *J. Environ. Chem. Eng.* 7 (2019). doi:10.1016/j.jece.2019.103376.
- [10] L. Ilieva, P. Petrova, G. Pantaleo, R. Zanella, J.W. Sobczak, W. Lisowski, I. Ivanov, Z. Kaszkar, L.F. Liotta, A.M. Venezia, T. Tabakova, Impact of ceria loading on the preferential CO oxidation over gold catalysts on CeO₂/Al₂O₃ and Y-doped CeO₂/Al₂O₃ supports prepared by mechanical mixing, *Catal. Today.* 357 (2020) 547–555. doi:10.1016/j.cattod.2019.06.006.
- [11] Z. Qiu, X. Guo, J. Mao, R. Zhou, The catalytic performance of isolated-dispersed Au on nanosized CeO₂ for CO preferential oxidation in H₂-rich stream, *Appl. Surf. Sci.*

481 (2019) 1072–1079. doi:10.1016/j.apsusc.2019.03.219.

- [12] I. Barroso-Martín, C. Alberoni, E. Rodríguez-Castellón, A. Infantes-Molina, E. Moretti, Recent advances in photo-assisted preferential CO oxidation in H₂-rich stream, *Curr. Opin. Green Sustain. Chem.* 21 (2020) 9–15.
doi:10.1016/j.cogsc.2019.07.008.
- [13] A. Infantes-Molina, A. Villanova, A. Talon, M.G. Kohan, A. Gradone, V. Morandi, A. Vomiero, E. Moretti, Au-Decorated Ce-Ti Mixed Oxides for Efficient CO Preferential Photooxidation, *Appl. Mater. Interfaces.* 12 (2020) 38019–38030.
doi:10.1021/acsami.0c08258.
- [14] E. Rodríguez-Aguado, A. Infantes-Molina, A. Talon, L. Storaro, L. León-Reina, E. Rodríguez-Castellón, E. Moretti, Au nanoparticles supported on nanorod-like TiO₂ as catalysts in the CO-PROX reaction under dark and light irradiation: Effect of acidic and alkaline synthesis conditions, *Int. J. Hydrogen Energy.* 4 (2018) 923–936.
doi:10.1016/j.ijhydene.2018.11.050.
- [15] L.E. Gómez, J.F. Múnera, B.M. Sollier, E.E. Miró, A. V. Boix, Raman in situ characterization of the species present in Co/CeO₂ and Co/ZrO₂ catalysts during the CO-PROX reaction, *Int. J. Hydrogen Energy.* 41 (2016) 4993–5002.
doi:10.1016/j.ijhydene.2016.01.099.
- [16] A. Tavakoli, N. Nasiri, Y. Mortazavi, A.A. Khodadadi, Cyclic molecular designed dispersion (CMDD) of Fe₂O₃ on CeO₂ promoted by Au for preferential CO oxidation in hydrogen, *Int. J. Hydrogen Energy.* 45 (2020) 33598–33611.
doi:10.1016/j.ijhydene.2020.09.123.

- [17] S. Jampa, K. Wangkawee, S. Tantisriyanurak, J. Changpradit, A.M. Jamieson, T. Chaisuwan, A. Luengnaruemitchai, S. Wongkasemjit, High performance and stability of copper loading on mesoporous ceria catalyst for preferential oxidation of CO in presence of excess of hydrogen, *Int. J. Hydrogen Energy*. 42 (2017) 5537–5548. doi:10.1016/j.ijhydene.2016.08.078.
- [18] X. Guo, J. Mao, R. Zhou, Influence of the copper coverage on the dispersion of copper oxide and the catalytic performance of CuO/CeO₂(rod) catalysts in preferential oxidation of CO in excess hydrogen, *J. Power Sources*. 371 (2017) 119–128. doi:10.1016/j.jpowsour.2017.10.055.
- [19] A.R. Miranda Cruz, E.M. Assaf, J.F. Gomes, J.M. Assaf, New insights about the effect of the synthesis method on the CuO-CeO₂ redox properties and catalytic performance towards CO-PROX reaction for fuel cell applications, *J. Environ. Manage.* 242 (2019) 272–278. doi:10.1016/j.jenvman.2019.04.074.
- [20] C.G.M. Reis, K.A. Almeida, T.F. Silva, J.M. Assaf, CO preferential oxidation reaction aspects in a nanocrystalline CuO/CeO₂ catalyst, *Catal. Today*. 344 (2020) 124–128. doi:10.1016/j.cattod.2018.10.037.
- [21] Q. Zou, Y. Zhao, X. Jin, J. Fang, D. Li, K. Li, J. Lu, Y. Luo, Ceria-nano supported copper oxide catalysts for CO preferential oxidation: Importance of oxygen species and metal-support interaction, *Appl. Surf. Sci.* 494 (2019) 1166–1176. doi:10.1016/j.apsusc.2019.07.210.
- [22] J. Lu, J. Wang, Q. Zou, D. He, L. Zhang, Z. Xu, S. He, Y. Luo, Unravelling the Nature of the Active Species as well as the Doping Effect over Cu/Ce-Based

- Catalyst for Carbon Monoxide Preferential Oxidation, *ACS Catal.* 9 (2019) 2177–2195. doi:10.1021/acscatal.8b04035.
- [23] A.R. Miranda Cruz, E.M. Assaf, J.F. Gomes, J.M. Assaf, Active copper species of co-precipitated copper-ceria catalysts in the CO-PROX reaction: An in situ XANES and DRIFTS study, *Catal. Today*. in press (2020). doi:10.1016/j.cattod.2020.09.007.
- [24] C. Xu, S. Li, Y. Zhang, Y. Li, J. Zhou, G. Qin, Synthesis of CuO_x–CeO₂ catalyst with high-density interfaces for selective oxidation of CO in H₂-rich stream, *Int. J. Hydrogen Energy*. 44 (2019) 4156–4166. doi:10.1016/j.ijhydene.2018.12.152.
- [25] G. Águila, F. Gracia, P. Araya, CuO and CeO₂ catalysts supported on Al₂O₃, ZrO₂, and SiO₂ in the oxidation of CO at low temperature, *Appl. Catal. A Gen.* 343 (2008) 16–24. doi:10.1016/j.apcata.2008.03.015.
- [26] J. Astudillo, G. Águila, F. Díaz, S. Guerrero, P. Araya, Study of CuO–CeO₂ catalysts supported on SiO₂ on the low-temperature oxidation of CO, *Appl. Catal. A Gen.* 381 (2010) 169–176. doi:10.1016/j.apcata.2010.04.004.
- [27] Y. Chen, Y. Liu, D. Mao, J. Yu, Y. Zheng, X. Guo, Z. Ma, Facile cyclodextrin-assisted synthesis of highly active CuO-CeO₂/MCF catalyst for CO oxidation, *J. Taiwan Inst. Chem. Eng.* In press (2020). doi:https://doi.org/10.1016/j.jtice.2020.07.015.
- [28] I.S. Tiscornia, A.M. Lacoste, L.E. Gómez, A. V Boix, CuO-CeO₂/SiO₂ coating on ceramic monolith: Effect of the nature of the catalyst support on CO preferential oxidation in a H₂-rich stream, *Int. J. Hydrogen Energy*. 45 (2020) 6636–6650. doi:10.1016/j.ijhydene.2019.12.126.

- [29] Á. Reyes-Carmona, A. Arango-Díaz, E. Moretti, A. Talon, L. Storaro, M. Lenarda, A. Jiménez-López, E. Rodríguez-Castellón, CuO/CeO₂ supported on Zr doped SBA-15 as catalysts for preferential CO oxidation (CO-PROX), *J. Power Sources*. 196 (2011) 4382–4387. doi:10.1016/j.jpowsour.2010.10.019.
- [30] C. Tang, J. Sun, X. Yao, Y. Cao, L. Liu, C. Ge, F. Gao, L. Dong, Efficient fabrication of active CuO-CeO₂/SBA-15 catalysts for preferential oxidation of CO by solid state impregnation, *Appl. Catal. B Environ.* 146 (2014) 201–212. doi:10.1016/j.apcatb.2013.05.060.
- [31] V. Meynen, P. Cool, E.F. Vansant, Verified syntheses of mesoporous materials, *Microporous Mesoporous Mater.* 125 (2009) 170–223. doi:10.1016/j.micromeso.2009.03.046.
- [32] W.J.J. Stevens, M. Mertens, S. Mullens, I. Thijs, G. Van Tendeloo, P. Cool, E.F. Vansant, Formation mechanism of SBA-16 spheres and control of their dimensions, *Microporous Mesoporous Mater.* 93 (2006) 119–124. doi:10.1016/j.micromeso.2006.02.015.
- [33] M. Kruk, M. Jaroniec, A. Sayari, Application of large pore MCM-41 molecular sieves to improve pore size analysis using nitrogen adsorption measurements, *Langmuir*. 13 (1997) 6267–6273. doi:10.1021/la970776m.
- [34] T. Benamor, L. Vidal, B. Lebeau, C. Marichal, Influence of synthesis parameters on the physico-chemical characteristics of SBA-15 type ordered mesoporous silica, *Microporous Mesoporous Mater.* 153 (2012) 100–114. doi:10.1016/j.micromeso.2011.12.016.

- [35] M. Mesa, L. Sierra, J. Patarin, J.-L. Guth, Morphology and porosity characteristics control of SBA-16 mesoporous silica. Effect of the triblock surfactant Pluronic F127 degradation during the synthesis, *Solid State Sci.* 7 (2005) 990–997. doi:10.1016/j.solidstatesciences.2005.04.006.
- [36] F. Kleitz, T. Kim, R. Ryoo, Phase Domain of the Cubic Im 3 h m Mesoporous Silica in the, *Langmuir.* 22 (2006) 440–445.
- [37] F. Rouquerol, J. Rouquerol, K.S.W. Sing, P. Llewellyn, G. Maurin, Adsorption by Powders and Porous Solids, second ed., Elsevier, Amsterdam, 2014. doi:10.1016/B978-0-08-097035-6.00007-3.
- [38] J.A. Cecilia, A. Arango-Díaz, F. Franco, J. Jiménez-Jiménez, L. Storaro, E. Moretti, E. Rodríguez-Castellón, CuO-CeO₂ supported on montmorillonite-derived porous clay heterostructures (PCH) for preferential CO oxidation in H₂-rich stream, *Catal. Today.* 253 (2015) 126–136. doi:10.1016/j.cattod.2015.01.040.
- [39] D. Gu, C.J. Jia, H. Bongard, B. Spliethoff, C. Weidenthaler, W. Schmidt, F. Schüth, Ordered mesoporous Cu-Ce-O catalysts for CO preferential oxidation in H₂-rich gases: Influence of copper content and pretreatment conditions, *Appl. Catal. B Environ.* 152–153 (2014) 11–18. doi:10.1016/j.apcatb.2014.01.011.
- [40] Wang, H. Pu, G. Wan, K. Chen, J. Lu, Y. Lei, L. Zhong, S. He, C. Han, Y. Luo, Promoted the reduction of Cu²⁺ to enhance CuO CeO₂ catalysts for CO preferential oxidation in H₂-rich streams: Effects of preparation methods and copper precursors, *Int. J. Hydrogen Energy.* 42 (2017) 21955–21968. doi:10.1016/j.ijhydene.2017.07.122.

- [41] Z. Zhang, K. Chen, J. Lu, Q. Zou, Y. Zhao, Y. Luo, D. He, R. Li, Sn-induced CuO–CeO₂ catalysts with improved performance for CO preferential oxidation in H₂-rich streams, *Int. J. Hydrogen Energy*. 46 (2021) 22508–22518.
doi:10.1016/j.ijhydene.2021.04.099.
- [42] Á. Szegedi, M. Popova, K. Lázár, S. Klébert, E. Drotár, Impact of silica structure of copper and iron-containing SBA-15 and SBA-16 materials on toluene oxidation, *Microporous Mesoporous Mater.* 177 (2013) 97–104.
doi:10.1016/j.micromeso.2013.04.024.
- [43] P.S. Barbato, A. Di Benedetto, G. Landi, L. Lisi, CuO/CeO₂ based monoliths for CO preferential oxidation in H₂-rich streams, *Chem. Eng. J.* 279 (2015) 983–993.
doi:10.1016/j.cej.2015.05.079.
- [44] L. Yang, S. Zhou, T. Ding, M. Meng, Superior catalytic performance of non-stoichiometric solid solution Ce_{1-x}Cu_xO_{2-δ} supported copper catalysts used for CO preferential oxidation, *Fuel Process. Technol.* 124 (2014) 155–164.
doi:10.1016/j.fuproc.2014.03.002.
- [45] M. Konsolakis, The role of Copper–Ceria interactions in catalysis science: Recent theoretical and experimental advances, *Appl. Catal. B Environ.* 198 (2016) 49–66.
doi:10.1016/j.apcatb.2016.05.037.
- [46] P. Gaudin, P. Fioux, S. Dorge, H. Nouali, M. Vierling, E. Fiani, M. Molière, J.-F. Brilhac, J. Patarin, Formation and role of Cu⁺ species on highly dispersed CuO/SBA-15 mesoporous materials for SO_x removal: An XPS study, *Fuel Process. Technol.* 153 (2016) 129–136. doi:10.1016/j.fuproc.2016.07.015.

- [47] F. Larachi, J. Pierre, A. Adnot, A. Bernis, Ce 3d XPS study of composite Ce Mn $1-x$ O $2-y$ wet oxidation catalysts, *Appl. Surf. Sci.* 195 (2002) 236–250.

Supplementary Materials

CuO-CeO₂ catalysts based on SBA-15 and SBA-16 for COPrOx. Influence of oxides concentration, incorporation method and support structure.

Inés S. Tiscornia^{a*}, Albano M. Lacoste^a, Magali Bonne^{b,c}, Bénédicte Lebeau^{b,c}, Alicia V. Boix^a

^aInstituto de Investigaciones en Catálisis y Petroquímica, INCAPE (FIQ, UNL-CONICET), 3000 Santa Fe, Argentina.

^bUniversité de Haute Alsace (UHA), CNRS, IS2M UMR 7361, 68100 Mulhouse, France.

^cUniversité de Strasbourg, F-67000 Strasbourg, France.

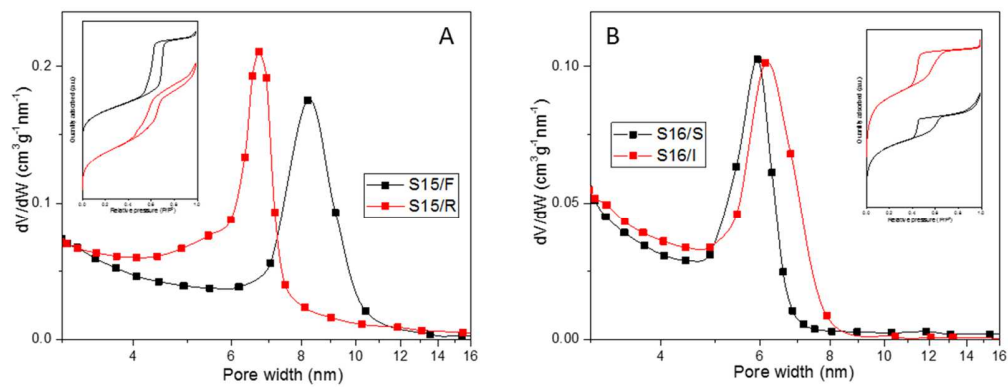


Figure S1. PSD (BJH-KJS method) and nitrogen adsorption isotherms of silica supports. (A) S15/F and S15/R, (B) S16/S and S16/I.

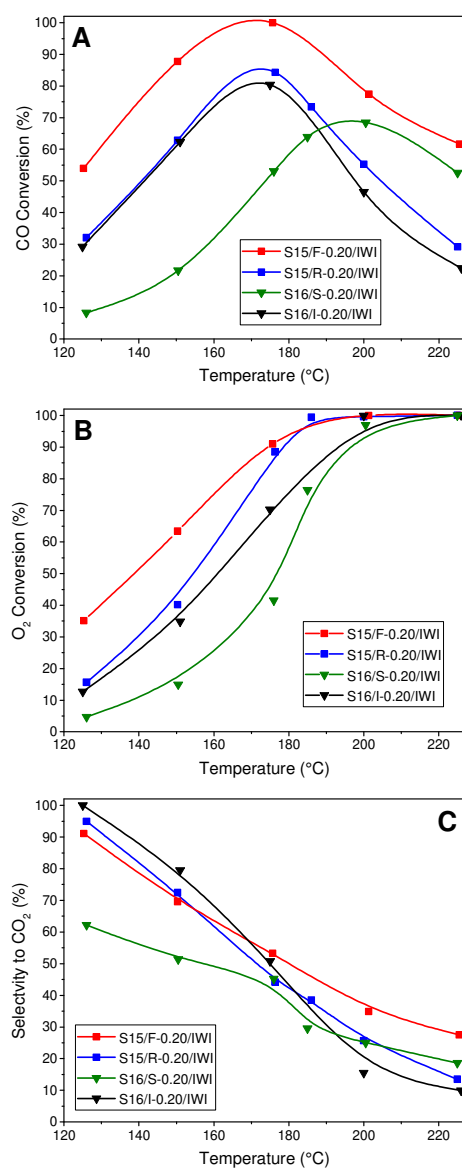


Figure S2. CO conversion (A), O₂ conversion (B) and selectivity to CO₂ (C) curves of catalysts obtained by IWI method. Reaction conditions: 1% CO, 1% O₂, 40% H₂ in He balance; $\tau = 0.138 \text{ g}_{\text{cat}} \text{ s mL}^{-1} \text{ STP}$.

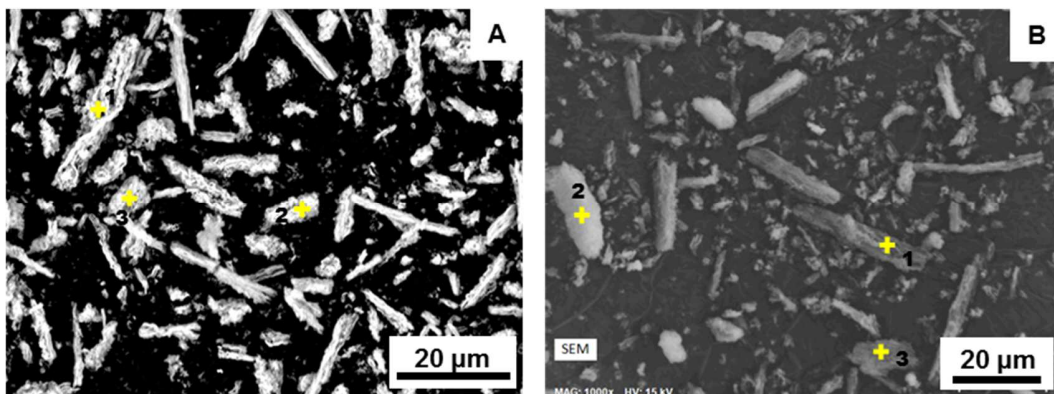


Figure S3. SEM image and EDS spots of (A) S15/F-0.20/IWI catalyst, molar fraction (1) Si/Ce/Cu=0.88/0.073/0.051, (2) Si/Ce/Cu=0.88/0.075/0.053, (3) Si/Ce/Cu=0.87/0.068/0.046; (B) S15/F-0.20/SSI (1) Si/Ce/Cu=0.87/0.034/0.08, (2) Si/Ce/Cu=0.78/0.139/0.07, (3) Si/Ce/Cu=0.79/0.098/0.11. Nominal molar fraction Si/Ce/Cu = 0.88/0.075/0.042 (considering Si, Ce and Cu, excluding O).

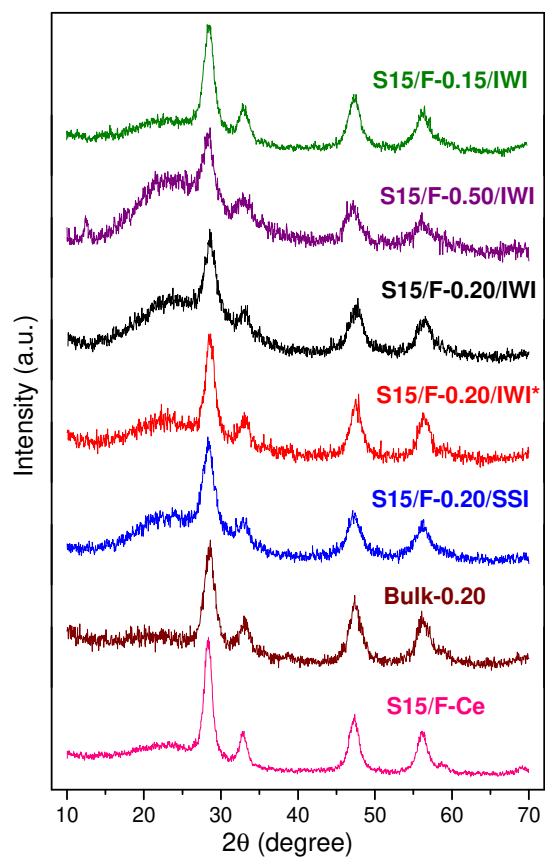


Figure S4. X-ray diffraction of the catalysts based on SBA-15 fibers, Bulk 0.20 and S15/F-Ce.

Table S1. XRD parameters of catalysts based on SBA-15 fibers, Bulk-0.20 and S15/F-Ce.

Catalysts	Lattice parameter (nm)	Crystallite size (nm)
S15/F-0.15/IWI	0.54351	5.3
S15/F-0.20/IWI	0.54122	5.5
S15/F-0.50/IWI	0.54445	5.3
S15/F-0.20/IWI*	0.54039	5.6
S15/F-0.20/SSI	0.54418	4.5
S15/F-Ce	0.54514	6.6
Bulk-0.20	0.54184	4.8